JGR Oceans

RESEARCH ARTICLE
10.1029/2021JC017982

Mechanisms Controlling the Distribution of Net Water Transport in Estuarine Networks

Jinyang Wang[1], **Yoeri M. Dijkstra**[2], **and Huib E. de Swart**[1]

[1]Institute for Marine and Atmospheric Research Utrecht (IMAU), Utrecht University, Utrecht, The Netherlands, [2]Delft Institute of Applied Mathematics, Delft University of Technology, Delft, The Netherlands

Key Points:

- Using a 2DV exploratory model, net water transport is disentangled into different components and attributed to their driving mechanisms
- The theory of differential water level setup is extended to explain net water transport due to these various driving mechanisms
- In the Yangtze Estuary, net water transport due to tidal rectifications and density gradients can be comparable to river water transport

Supporting Information:

Supporting Information may be found in the online version of this article.

Correspondence to:

J. Wang,
j.wang@uu.nl;
jinyang.wang27@outlook.com

Citation:

Wang, J., Dijkstra, Y. M., & de Swart, H. E. (2022). Mechanisms controlling the distribution of net water transport in estuarine networks. *Journal of Geophysical Research: Oceans*, *127*, e2021JC017982. https://doi.org/10.1029/2021JC017982

Received 8 SEP 2021
Accepted 16 DEC 2021

Author Contributions:

Conceptualization: Jinyang Wang, Yoeri M. Dijkstra, Huib E. de Swart
Supervision: Yoeri M. Dijkstra, Huib E. de Swart
Writing – review & editing: Jinyang Wang, Yoeri M. Dijkstra, Huib E. de Swart

Abstract Net water transport (NWT) in estuaries is important for, for example, salt intrusion and sediment dynamics. While NWT is only determined by river runoff in single channels, in estuarine networks, it results from a complex interplay between tides and residual flows. This study aims to disentangle the various contributions of these physical drivers to NWT in estuarine networks and investigate the sensitivities of NWT to variable forcing conditions, interventions, and sea level rise (SLR). To this end, a processes-based perturbative network model is developed, which accounts for the vertical flow structure to resolve density-driven flow driven by a vertically uniform along-channel salinity gradient. Other identified drivers are river discharge and three tidal rectification processes: Stokes transport and its return flow, momentum advection, and velocity-depth asymmetry. The model is applied to the Yangtze Estuary. NWT due to tidal rectifications and density-driven flow can be comparable to river discharge. Specifically in the North Branch, the direction of NWT may differ from the direction of river discharge. Varying river discharge mainly affects NWT as tide-river interaction is weak and density-driven flow is shown to be insensitive to salt intrusion. Conversely, variations in tidal amplitude strongly affect NWT related to tidal rectification and density-driven flow. The deepening (narrowing) of one channel (Deep Waterway Project), affected the NWT mostly through the density-driven flow (advection). Furthermore, NWT distribution in the Yangtze is insensitive to SLR up to 2 m because the effects of SLR on transport due to different drivers compensate each other.

Plain Language Summary To complement numerical models, a partly analytical model is used to decompose net water transport in estuarine networks into different components according to their driving physical processes related to river discharge, differences in water density, and tidal rectification. Applying the model to the Yangtze Estuary (China), this study demonstrates the dependence of each component of net water transport on external forcing conditions (river and tide), as well as their sensitivity to local human intervention and sea level rise. Previous understanding of the tidal influence on net water transport is generalized to explain the creation of net water transport by arbitrary physical processes in estuarine networks.

1. Introduction

Knowledge of net (i.e., subtidal) water transport (NWT) in estuaries is important because it strongly impacts water quality and ecological processes (Cloern et al., 2016). For a single-channel estuary in equilibrium, the net transport is determined by the river run off. However, many systems like the Yangtze Estuary (China), the Pearl Estuary (China), and the Mahakam Delta (Indonesia) consist of multiple channels. In such estuarine networks, water from different channels is exchanged at junctions or branching points. It has been shown that this distribution of the NWT in networks not only depends on river run off, but also on density differences and tidal amplitude, making it highly complex (Alebregtse & de Swart, 2016; Hoitink & Jay, 2016). To better understand the NWT and its sensitivity to river discharge and tides, it is useful to disentangle the contributions by these various physical drivers.

NWT in estuarine networks has received considerable attention (e.g., Buschman et al., 2010; Li et al., 2010; Ridderinkhof, 1988; Sassi et al., 2011; Wu et al., 2006; W. Zhang et al., 2017) and several methods exist for disentangling the different contributions to it. One such approach is the factor separation method (Stein & Alpert, 1993), which makes it possible to distinguish the effects of rivers, tides, and their interactions on net transport from numerical model results. Using this method, Sassi et al. (2011) proposed the framework of *differential water level setup* to explain the effect of tides on NWT: river-tide interactions alter the subtidal water level in one channel, adjusting the pressure gradient in the adjacent channels and thus leading to a reallocation of NWT at the

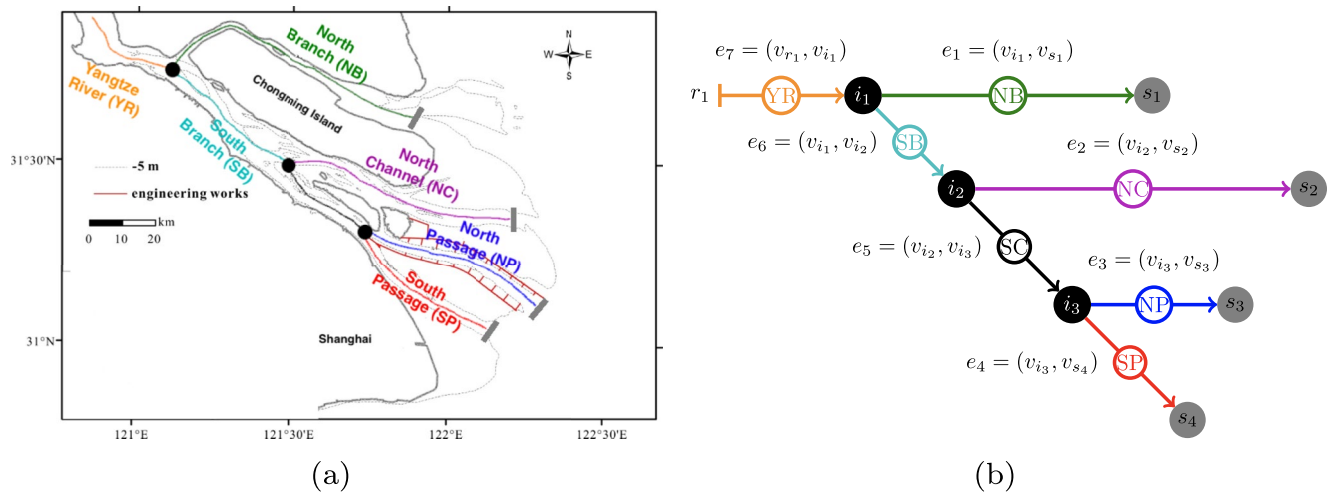

Figure 1. (a) Map of the Yangtze Estuary (YE) adapted from (Jiang et al., 2013). (b) The diagram that represents the channel network of the YE. Solid gray circles denote open sea where tidal forcing is prescribed. The closed ends of river channels are shown in vertical bars, where tidal current vanishes and a constant river discharge is prescribed. Each color circle encloses the abbreviation for that channel.

junction. However, the factor separation method is not suitable for disentangling more contributions to subtidal transport, such as baroclinicity and several distinct contributions generated by tides. Alternatively, Alebregtse and de Swart (2016) present a framework for disentangling the various contributions of tidal rectification on NWT in estuarine tidal networks using perturbation expansions. They used a process-based 1D model and identified the contributions by river discharge, Stokes transport and the associated return flow, horizontal advection within channels and at junctions, and depth-dependent friction. They showed that each of these contributions is responsible for generating NWT in channels of an estuarine network. However, because of the 1D nature of their model, subtidal flow due to for example, vertical advection of horizontal momentum and density-driven flow are missing. The latter is considered to be one of the strongest contributors to subtidal flows in many tidal channels, for example, in the North Passage of the Yangtze Estuary (Jiang et al., 2013).

The goal of this study is to disentangle and analyze the contributions of different drivers for the distribution of NWT in estuarine networks including density-driven flow and vertical advection and investigate their sensitivity to river discharge, tide, human interventions, and sea level rise. To this end, the idealized process-based 2DV network model by J. Wang et al. (2021) is extended in two aspects. First, tidal rectifications are taken into account. Second, the effect of the along-channel density gradient is considered, as well as its impact on vertical eddy viscosity parameterization. Furthermore, it will be shown that our method naturally extends the conceptual framework of differential water level setup of Sassi et al. (2011).

The prototype estuarine network that is considered in this study is the Yangtze Estuary (YE), China, for which the network model by J. Wang et al. (2021) has been calibrated. The model yields characteristics of tides that agree fairly well with field data. The water motion in the YE is primarily forced by the river discharge from the Yangtze River and tides from the East China Sea (Figure 1). The YE is a good example for studying sensitivity of NWT to variable forcing conditions, as it is an estuary network characterized by a significant seasonal river discharge variation and spring-neap modulation (Yang et al., 2015). Moreover, the geometric characteristics of the YE have been changed in the past century due to both natural and anthropogenic reasons, which in turn lead to the change in the distribution of NWT over channels. To give a deeper insight into the effect of the various interventions and changes on the NWT, two cases will be studied. First, we will assess the relative impact of the Deep Waterway Project that comprised both the narrowing and deepening of the North Passage. Second, the effects of sea level rise on the drivers of the distribution of NWT will be investigated. While the aim of this study is qualitative, the computed NWT will be compared to other studies that aimed at a more precise quantitative estimate of NWT to verify the results and add a deeper process-level understanding of these numbers.

This manuscript is structured as follows. Section 2 presents the model geometry and outlines the derivation of equations that govern the subtidal dynamics in estuarine networks. The model is then applied to the Yangtze Estuary and the motivation for the design of experiments is outlined. The results showing the response of NWT

in the Yangtze Estuary to different changes are contained in Section 3. This motivates the physical mechanism that explains the generation of NWT in estuarine network, which is explained in the discussion (Section 4) and followed by the conclusions (Section 5).

2. Model and Methods

2.1. Model

2.1.1. Domain and Graph Representation of a Network

In this study, the estuarine network is schematized as a set of connected idealized channels, which can be mathematically denoted as a directed graph $G = \{V, E\}$. The notation used here is consistent with the graph theory and hence slightly deviates from the notation of, for example, Hill and Souza (2006). An example for the Yangtze Estuary is given in Figure 1, where channel labeling is explained. The graph consists of a set of vertices V and edges E. The direction of each edge denotes the direction of the positive x-axis. The set of vertices V contains vertices marking river heads V_R, vertices connecting to the sea V_S, and internal vertices (junctions) V_I. Similarly, the set of edges E contains river channels E_R, sea channels E_S, and internal channels E_I. Each edge $e_j \in E$ is an ordered set of two vertices, marking the up- and downstream ends of the channels, so that an edge may be denoted as $e_j \equiv e_{qr} = (v_q, v_r)$ if the edge runs from v_q to v_r, with j the channel label. The Cartesian coordinates x and z are used, where x is the along-channel coordinate increasing in the direction of the river flow (seaward) and z is the vertical coordinate pointing upward, with $z = 0$ the undisturbed water level.

For each channel e_j, the length is denoted by L_j, and the depth H_j is assumed constant. The width is assumed depth-independent and exponential,

$$b_j(x) = b(L_j)\exp\left(\frac{x - L_j}{l_{b,j}}\right), \quad 0 \le x \le L_j, \forall e_j \in E. \tag{1}$$

Here, $l_{b,j}$ is the length scale at which the width of channel e_j varies exponentially. Channel indices will be omitted in the rest of this manuscript for equations that hold for all channels.

2.1.2. Equations of Motion

The water motion is governed by the width-averaged shallow water equations. These equations can be decomposed into different harmonic components, assuming that every state variable can be represented by a superposition of a truncated harmonic series. The harmonic component of a state variable, or a term, is denoted by a subscript n. The truncated harmonic series contain the subtidal frequency ($n = 0$) and the semi-diurnal frequency (i.e., M_2, $n = 1$). Detailed explanation is provided in Supporting Information S1. The resulting equations are

$$\frac{\partial u_n}{\partial t} + \left(u\frac{\partial u}{\partial x} + w\frac{\partial u}{\partial z}\right)_n = -g\frac{\partial \eta_n}{\partial x} - \left(\frac{g}{\rho_0}\int_z^\eta \frac{\partial \rho}{\partial x} dz'\right)_n + \breve{A}_{vn}\frac{\partial^2 u_n}{\partial z^2}, \tag{2a}$$

$$\frac{\partial u_n}{\partial x} + \frac{\partial w_n}{\partial z} + \frac{1}{l_b}u_n = 0, \tag{2b}$$

where η is the free surface height, u is the along channel velocity, w is the vertical velocity, and the gravitational acceleration $g = 9.81$ m/s^2. Note that in the advective term, the total velocity contains all frequencies, only the relevant frequencies are retained after the nonlinear interaction. For the constant vertical eddy viscosity $\breve{A}_{vn}$, the subscript n denotes the eddy viscosity acting on the harmonic component n. The magnitude of eddy viscosity is different for tidal and subtidal flows, as discussed in detail in the next subsection. Water density ρ varies due to vertically well-mixed tidally averaged salinity $s(x)$ as

$$\rho = \rho_0(1 + \beta_s s), \tag{3}$$

where the saline contraction coefficient $\beta_s = 8.3 \times 10^{-4}$ psu^{-1} and $\rho_0 = 1{,}000$ kg/m^3 is the reference density. As can be seen from the second term on the right-hand side of Equation 2a, this density field creates a depth-dependent (so baroclinic) pressure gradient force. The longitudinal salinity profile in each channel is described by the subtidal salt mass balance in equilibrium:

$$\frac{\mathrm{d}}{\mathrm{d}x}(T_s) = 0, \quad T_s = Qs - bHK_h\frac{\mathrm{d}s}{\mathrm{d}x}. \tag{4}$$

Here, Q is the net water transport (NWT, see also Section 2.1.4), K_h is the horizontal eddy diffusivity, and T_s is the cross-sectionally averaged salt transport, which is a constant for each channel.

The boundary conditions to Equation 2 at the free surface $z = \eta$ are the no stress condition and the kinematic boundary condition. The bottom $z = -H$ is assumed to be impermeable and a partial-slip condition (Engelund, 1970) is applied, i.e.,

$$\check{A}_{vn}\frac{\partial u_n}{\partial z} = 0 \quad \text{and} \quad w_n = \frac{\partial \eta_n}{\partial t} + \left(u\frac{\partial \eta}{\partial x}\right)_n \quad at \;\; z = \eta_n, \tag{5a}$$

$$\check{A}_{vn}\frac{\partial u_n}{\partial z} = \check{s}_{fn}u_n \;\text{ and }\; w_n = 0 \qquad at\; z = -H, \tag{5b}$$

where $\check{A}_{vn}\frac{\partial u_n}{\partial z}$ is the kinematic internal stress and $\check{s}_{fn}$ are the constant slip parameter, whose value differs for each harmonic component (see Section 2.1.3 for more details). At the seaside vertices $v \in V_S$, the water motion is forced by a prescribed sea surface elevation and a subtidal salinity is prescribed. At river head vertices $v \in V_R$, a constant river discharge is imposed and the salinity is assumed to vanish, viz.

$$\eta_{n,j} = \delta_{n1}Z_j\cos(\omega t - \phi_j) \;\text{ and }\; s_j = s_{\text{sea},j} \qquad \text{at}\;\; x = L_j, \forall e_j \in Es, \tag{6a}$$

$$b_j\int_{-H_j}^{\eta_j} u_{n,j}\,dz = \delta_{n0}Q_{R,j} \;\text{ and }\; s_j = 0 \qquad \text{at}\;\; x = 0, \quad \forall e_j \in E_R, \tag{6b}$$

where ω is the angular frequency for the M_2 tide, Z_j, ϕ_j and s_{sea} are the prescribed tidal amplitudes, phases and salinity at the open sea, Q_R is the constant river discharge, and δ_{nk} is the Kronecker delta ($\delta_{nk} = 1$ if $n = k$ and 0 otherwise). When $n = 0$, the subtidal water level is 0 at the sea and a volume flux (river discharge) is prescribed at the river head. When $n = 1$, the water level at the sea is periodic (M_2) and the cross-sectionally integrated tidal current vanishes at the tidal limit.

At each vertex $v \in V_I$, conservation of mass is assumed for water motion. From the momentum balance, it follows a condition for the depth-averaged dynamic pressure, which is discussed in Section S5 in the Supporting Information S1. Salinity is assumed to be continuous and salt mass transport is assumed to be conserved. These conditions read

$$g\eta_{n,j} + \frac{\mu}{2}\left(\overline{u_j^2}\right)_n = g\eta_{n,k} + \frac{\mu}{2}\left(\overline{u_k^2}\right)_n \quad \text{and} \quad s_j = s_k, \qquad \forall v_i \in V_I,\; \forall j,k \;\text{ such that }\; v_i \in e_j, e_k, \tag{7a}$$

$$\sum_{e_j \in I_i} b_j H_j \overline{u_j} = \sum_{e_j \in O_i} b_j H_j \overline{u_j} \quad \text{and} \quad \sum_{e_j \in I_i} T_{s,j} = \sum_{e_j \in O_i} T_{s,j}, \qquad \text{for sets}\;\; I_i = \{e \in E | e = (v_q, v_i)\} \quad \text{and} \quad O_i = \{e \in E | e = (v_i, v_q)\}, \tag{7b}$$

where a bar $\bar{\cdot}$ denotes the average over depth, and μ is the fraction of kinetic energy dissipated at the junction (van de Kreeke, 1988). Equation 7b, describing mass conservation for both water and salt at junctions, differentiates between the set of channels downstream of a junction O_i and the set of channels upstream of a junction I_i. In this study, upstream and downstream are defined with respect to the negative and positive x-directions.

2.1.3. Turbulence Model

The values of the effective eddy viscosity and slip parameter are generally different for each harmonic component (Godin, 1999). These values are computed assuming that in each channel, the total energy dissipation due to viscous effects over one tidal cycle at each frequency is the same as the energy dissipation obtained from a space- and time-dependent turbulence model. The space- and time-dependent turbulence model used here is extended compared to J. Wang et al. (2021) to account for the effect of periodic density stratification on eddy viscosity (Jiang et al., 2013):

$$A_v(x,z,t) = l^2 \left|\frac{\partial u}{\partial z}\right| \left(1 + \left|\frac{\partial \rho}{\partial x}\right| \frac{|\hat{u}_1|}{\omega \Delta\rho} \cos(\omega t - \alpha)\right). \tag{8}$$

Here, $\Delta\rho$ is the vertical density difference scale (fixed on input) and $\hat{u}_1$ is the complex amplitude of the M_2 velocity (computed in the model). Note that the vertical density stratification is considered here, but not in the momentum equation Equation 2a. This is because the contribution to salinity gradient by the vertical variation in salinity is much smaller than the depth-averaged salinity (Pritchard, 1954). Additionally, α is the phase difference between the M_2 velocity and the M_2 eddy viscosity. Its value is chosen such that the M_2 eddy viscosity attains maximum at the end of flood. The mixing length l (Kundu et al., 2016), which contains a calibration parameter, is parametrised by a parabolic profile adapted from Chen and de Swart (2016) and is the same as that used by J. Wang et al. (2021). The partial slip parameter in the space- and time-dependent turbulence closure is assumed to be linear in the local bottom velocity magnitude $|u_b|$,

$$s_f = C_{100} |u_b|, \tag{9}$$

where C_{100} is the bottom drag coefficient, the value of which depends on the bottom type and typically ranges from 0.001 to 0.006 (Soulsby, 1997).

2.1.4. Net Water Transport

Denoting the time average over one tidal cycle by $\langle\cdot\rangle$, the NWT Q is defined to be the tidally-averaged volumetric flow rate, i.e.,

$$Q = \left\langle b(x) \int_{-H}^{\eta} u\,dz \right\rangle = b\left(\int_{-H}^{0} \langle u\rangle\ dz + \left\langle \int_{0}^{\eta} u\,dz \right\rangle\right) \approx b\left(\int_{-H}^{0} \langle u\rangle\ dz + \langle \eta u|_{z=0}\rangle\right). \tag{10}$$

On the right hand side, the first term is the transport up to the mean sea level $z = 0$. The second term is the correction to the transport due to free surface variations and follows from the first term in the power series of u about $z = 0$, provided that the free surface variation is much smaller than the mean water depth.

2.2. Construction of Approximate Solutions

Approximate solutions of the system (Equations 2–7) are constructed using the perturbation method (as detailed in the Supporting Information S1). Equations are nondimensionalized, scaled, and written in terms of asymptotic expansions of state variables in a small parameter ε. Here, ε is the ratio of prescribed tidal elevation amplitude to the undisturbed water depth (Ianniello, 1977; Ianniello, 1979). Next, state variables are written in terms of an asymptotic series

$$u_n = u_n^0 + u_n^1 + \cdots, \tag{11}$$

and similar for η and w, where the superscript denotes the order of ε. Collecting terms at the same order of ε results in a system of equations at each order of ε. The leading order system and the associated solutions, featuring the M_2 tidal motion and river flow, are identical to that of J. Wang et al. (2021). The first-order solutions are developed below.

Focusing on the subtidal flow, the solution procedure allows for distinguishing several contributions. At the leading-order, there is only the contribution by the river discharge. At the first order, we obtained linear equations for the momentum and depth-integrated continuity equations that read as

$$g\frac{d\eta_0^1}{dx} - \check{A}_{v0}^{\,0}\frac{\partial^2 u_0^1}{\partial z^2} = \underbrace{\sum_n -\left\langle u_n^0 \frac{\partial u_n^0}{\partial x} + w_n^0 \frac{\partial u_n^0}{\partial z}\right\rangle}_{F_{\text{adv}}} + \underbrace{\frac{g}{\rho_0}\frac{d\rho}{dx} z}_{F_{\text{baroc}}} + \underbrace{\check{A}_{v0}^{\,1}\frac{\partial^2 u_0^0}{\partial z^2}}_{F_{\text{rivc}}}, \tag{12a}$$

$$b(x)\left(\int_{-H}^{0} u^1\,dz + \underbrace{\sum_n \left\langle \eta_n^0 u_n^0|_{z=0}\right\rangle}_{F_{\text{Stokes}}}\right) = Q^1, \tag{12b}$$

where Q^1 is the first order contribution to the subtidal transport. It turns out that the eddy viscosity and slip parameter acting on the first order flow are the same as those acting on the leading order flow. All terms denoted by underbraces only involve known quantities from the leading-order solution. Detailed physical interpretations of these terms are provided in Section 2.3. These equations are linear in the first-order unknowns u_0^1 and η_0^1. Therefore the superposition principle can be applied to decompose the subtidal system: the solutions are constructed by adding contributions of different forcing mechanisms (Ianniello, 1977). The forcing terms are indicated by an underbrace: F_{adv} is the momentum advection by the leading-order flow, F_{Stokes} is the Stokes transport, F_{rivc} is a first order correction to the river flow and F_{baroc} is the baroclinic forcing. The boundary conditions at the mean sea surface and bottom, respectively, read

$$\check{A}_{v0}{}^0 \frac{\partial u_0^1}{\partial z} = -\underbrace{\sum_n \left\langle \eta_n^0 \frac{\partial^2 u_n^0}{\partial z^2}\right\rangle}_{F_{\text{vda}}} \qquad \text{at } z = 0, \tag{13a}$$

$$\check{A}_{v0}{}^0 \frac{\partial u_0^1}{\partial z} - \check{s}_{f0}^0 u_0^1 = 0 \qquad \text{at } z = -H, \tag{13b}$$

At the free surface, the additional term $\left\langle \eta_n^0 \frac{\partial^2 u_n^0}{\partial z^2}\right\rangle$ is the result of Taylor expansion of the no-stress condition about $z = 0$. It is interpreted as the velocity-depth asymmetry (F_{vda}, see Section 2.3). The first-order horizontal boundary conditions describe no additional tidal forcing at the seaward boundary and no additional river discharge at the landward boundary. Furthermore, we require the continuity of momentum and mass, i.e.,

$$\eta_{0,j}^1 = 0 \qquad \text{at } x = L_j, \forall e_j \in E_S, \tag{14a}$$

$$b_j \int_{-H_j}^{0} u_{0,j}^1\,dz = 0 \qquad \text{at } x = 0, \quad \forall e_j \in E_R, \tag{14b}$$

$$g\eta_{0,j}^1 + \underbrace{\frac{\mu}{2}\sum_n \left\langle \overline{\left(u_{n,j}^0\right)^2}\right\rangle}_{F_{\text{dp}}} = g\eta_{0,k}^1 + \underbrace{\frac{\mu}{2}\sum_n \left\langle \overline{\left(u_{n,k}^0\right)^2}\right\rangle}_{F_{\text{dp}}}, \quad \text{at vertices,} \tag{14c}$$

$$\text{i.e. } \forall v_i \in V_I, \forall j,k \text{ s.t. } v_i \in e_j, e_k,$$

$$\sum_{e_j \in I_i} Q_{0,j}^1 = \sum_{e_j \in O_i} Q_{0,j}^1, \qquad \text{at vertices,} \tag{14d}$$

$$\text{i.e. for sets } I_i = \{e \in E | e = (v_q, v_i)\} \quad \text{and} \quad O_i = \{e \in E | e = (v_i, v_q)\}.$$

Here, F_{dp} is the forcing that creates first order subtidal flow in each channel such that the leading order momentum transfer is continuous, that is, continuous dynamic pressure. In order to determine the eddy viscosity and slip parameter, a perturbation method is also applied to the space- and time-dependent turbulence closure (see Section S3 in the Supporting Information S1 for details).

Equations 12–14 are linear inhomogeneous equations for each forcing term F, which can be solved independently. Therefore, the first order velocity can be written as,

$$u^1 = u^1_{\text{baroc}} + u^1_{\text{adv}} + u^1_{\text{Stokes}} + u^1_{\text{vda}} + u^1_{\text{dp}} + u^1_{\text{rivc}}. \tag{15}$$

Analytical solutions for the first order velocities are presented in Section S4 in the Supporting Information S1. Detailed derivation and solution procedure for a single channel can be found in the user manual of iFlow (Supporting Information S1 of Dijkstra et al., 2017).

2.3. Forcing Mechanisms of Different Drivers for Net Water Transport

It turns out that each of the forcing terms identified in Equations 12–14 contributes to the NWT in addition to the river flow at the leading order. Due to the linearity of the ordered equations, the NWT can be written as

$$Q = Q_{\text{river}} + Q_{\text{baroc}} + Q_{\text{adv}} + Q_{\text{Stokes}} + Q_{\text{vda}} + Q_{\text{dp}} + Q_{\text{rivc}}. \tag{16}$$

Each term in Equation 16 is the result of one type of subtidal forcing mechanism, which will be described with focus on the contribution by tide in this subsection. Note that the NWT in a single channel in equilibrium is the same as the imposed river discharge and other residual flows have zero contribution due to mass conservation (Cheng et al., 2010; Ianniello, 1979). In a network, however, any type of subtidal flow may contribute to the NWT and mass conservation is still fulfilled (Alebregtse & de Swart, 2016; Sassi et al., 2011). For example, a single channel with imposed river discharge cannot import water from the sea. In contrast, a sea channel in a network may import water from the sea because this amount of water can be exported back to the sea through other sea channels. It will be demonstrated in Section 4.1 how each of these forcing mechanisms contribute to the NWT. Note that the rectification processes (horizontal advection, Stokes transport and its return flow, velocity-depth asymmetry, and dynamic pressure) are forced by both leading order river and tidal flow, but the forcing by the tidal flow is dominant, on which below interpretations are based.

1. **River (F_{river})** The leading order approximation to the externally prescribed river discharge.
2. **Baroclinicity (F_{baroc})** The consequence of the salinity gradient, resulting in a density-driven flow.
3. **Advection (F_{adv})** Advection of the along-channel momentum, by both horizontal and vertical currents.
4. **Stokes transport (F_{Stokes})** Tidal flow is periodic and after each tidal cycle, there will be a net displacement of water particles in the direction of tidal wave propagation (Stokes drift). To satisfy mass conservation, this is compensated by a return flow that transports water in the opposite direction, which is forced by the Stokes transport. The sum of Stokes transport and the transport due to its return flow is a constant in each channel in a network.
5. **Velocity-depth asymmetry (F_{vda})** It is due to the correlation between free surface height and flow curvature at the free surface, which varies over one tidal cycle and so does the vertical profile of the velocity. The velocity at each depth is therefore not symmetric over one tidal cycle. It hence acts as depth-dependent friction on depth-averaged flow.
6. **Continuous dynamic pressure (F_{dp})** This contribution amounts to tidal rectification due to advection at junctions. It is the consequence of momentum conservation at junctions (see Section S5 in the Supporting Information S1 for more details).
7. **A correction to river flow (F_{rivc})** The friction parameters for the river flow are calculated assuming that they are only affected by the river and tidal flows. The influence of other subtidal flows on the friction parameters for the river flow is accounted for by this contribution. Physically, it is a correction to the river flow that parametrically accounts for the effect of periodic density stratification on vertical mixing.

2.4. Design of Experiments and Parameter Values

The reference case for this study is the Yangtze Estuary in the dry season (January 2014), to which the model has been calibrated to yield characteristics of both rivers and tides that agree fairly well with field data (J. Wang et al., 2021). Analysis of the turbulence model shows that (as detailed in Section S3 in the Supporting Information S1) the additional term in Equation 8 that accounts for the density stratification in vertical eddy viscosity only has influence on the subtidal dynamics and hence new calibration is not required. The typical density difference $\Delta\rho$ between the bottom and the surface is about 7 kg/m^3 (Jiang et al., 2013). Table 1 contains the geometric characteristics of each channel. Water motion is forced from both the seaward and landward boundaries. At the sea, a constant river discharge $Q_R = 10^4$ m^3/s is imposed and the monthly averaged semidiurnal lunar tide (M_2) is prescribed at the sea (Table 1). The effects of seasonal variation in river discharge, spring-neap modulation, channel deepening/narrowing, and sea level rise on the distribution of NWT over different channels will be investigated by varying the prescribed discharge, tidal amplitudes, local channel depth/convergence, and water depth in all channels so that the sensitivity of water transport distributions to these changes can be investigated. The list of experiments is provided in Table 2. Head loss is not accounted for in this study and hence $\mu = 1$, meaning that there is no kinetic energy dissipation at junctions. The bottom drag coefficient C_{100} is 0.0022 (J. Wang et al., 2021).

Table 1
Geometry and M_2 Tidal Forcing of the Reference Yangtze Estuary Network, Including the Channel Length L, the Length Scale l_b at Which Channel Width Increases Exponentially in the Seaward Direction, the Water Depth H, and the Width at the Seaward Boundary b_o

Channel	Label	L (km)	l_b (km)	H (m)	b_o (km)
North Branch (NB)	1	85	30	5	12
North Channel (NC)	2	60	52	7	20
North Passage (NP)	3	61	470	11	3.5
South Passage (SP)	4	54	21	7	30
South Channel (SC)	5	23	−368	9	6.2
South Branch (SB)	6	51	64	9	14
Yangtze River 1 (YR1)	7	50	206	10	6.6
Yangtze River 2 (YR2)	8	50	206	10	5.2
Yangtze River 3 (YR3)	9	50	206	10	4.1
Yangtze River 4 (YR4)	10	50	206	10	3.2
Yangtze River 5 (YR5)	11	370	1,660	10	2.5

Channel	Elevation amplitude (m)	Elevation phase (rad)
NB	1.5	-0.53π
NC	1.06	-0.58π
NP	1.3	-0.58π
SP	1.3	-0.53π
Angular frequency ω	1.4×10^{-4} (s^{-1})	

The horizontal diffusion coefficient $K_h = 250$ m^2/s is used for all cases in the salt model. It will be shown and explained in Appendix A that the results for the NWT are insensitive to K_h.

The spring-neap variation is caused by the combination of M_2 and S_2 (semi-diurnal solar) tides, which may be seen as a slow (i.e., 14 days) modulation of the semidiurnal tide. While the term M_2 tide is used in this study, it represents all components with the semidiurnal (or D_2) period. For this reason, different phases of the spring-neap cycle are represented by varying the prescribed M_2 amplitudes at the sea. From neap to spring, the prescribed monthly averaged tidal amplitudes are multiplied by 0.5–1.5, as practical approximations, according to the observations by Lu et al. (2015).

Geometric characteristics in the North Passage (NP) were changed by the Deep Waterway Project (DWP) in two aspects: channel dredging that deepened the channel from 7 to 11 m and the construction of training walls, which increased the convergence length from 60 to 470 km, with the width at the junction unchanged. Their combined effect on NWT will be first investigated, followed by their individual effects.

Sea level rise (SLR) increases the mean water depth and thereby tidal amplitudes. The effects of changing tidal amplitudes have been investigated separately and therefore the SLR will be represented by increasing water

Table 2
List of Experiments

Section	Description	Changes
3.1	Reference	Dry season $Q_R = 1 \times 10^4$ m^3/s, monthly averaged tidal forcing (Table 1)
3.2	Wet season	Increase river discharge up to 4×10^4 m^3/s (Alebregtse & de Swart, 2016)
3.3	Spring-neap	Vary tidal amplitudes from 50% to 150% of the default case (Lu et al., 2015)
3.4	Before DWP	$H = 7$ m, $b_o = 3.5$ km and $l_b = 60$ km in the NP (Jiang et al., 2012)
3.5	Sea level rise	Increase undisturbed water depth up to 2 m (Kuang et al., 2017)

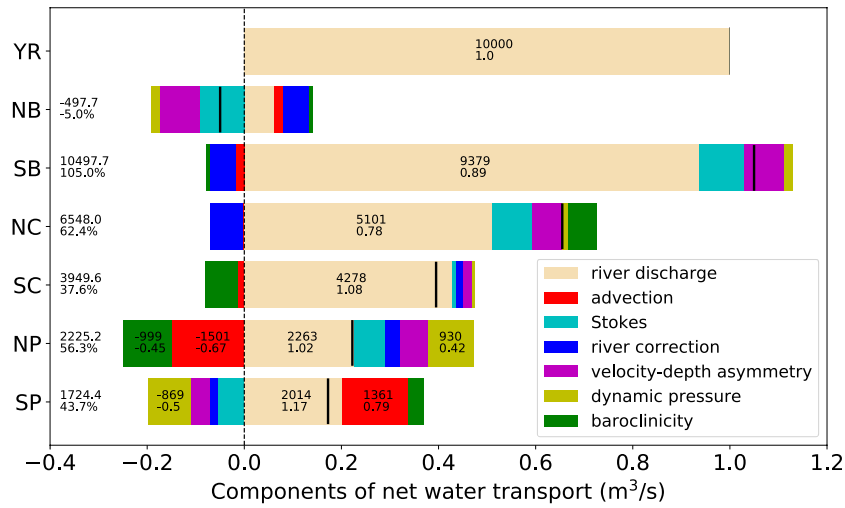

Figure 2. Net water transport (NWT) in the Yangtze Estuary for the reference case. Values on the left of each bar are the NWT (upper, m^3/s) and the net water diversion ratio (lower). Values within each box are the water transport of the component (upper) and the fraction of the component in the NWT. Values are hidden for fraction less than 20% and for the NB. In each channel, the magnitude of the NWT (the upper number on the left) is also indicated by a black vertical line.

depth. A reasonable upper bound for global SLR by 2100 would be 2 m (Nicholls et al., 2011), which was also used by Kuang et al. (2017) for the Yangtze Estuary. So the same upper bound for SLR will be used in this study.

To analyze the results, the distribution of the NWT over the different channels will be quantified by the net water diversion ratio (nWDR) (Li et al., 2010). At one junction, it is the ratio of the NWT in one downstream channel over the sum of NWTs in all downstream channels. In this study, there are at most two downstream channels connected by a junction and hence the nWDR reads

$$\text{nWDR} = \frac{Q_j}{Q_j + Q_k}, \quad \text{for} \quad e_j, e_k \in O_i, \tag{17}$$

where O_i is the set of all downstream channels of a branching point $v_i \in V_I$. The nWDRs of the North Branch, the North Channel, and the North Passage are sufficient for describing the distribution of NWT in the Yangtze Estuary, because the values for the other branching channels can be obtained by subtracting the nWDRs of these three channels from unity. In addition, using Equation 16, the nWDR can be further decomposed into different components according to the associated physical drivers.

3. Results

3.1. Reference Case

The modeled net water transport (NWT) for the reference case in all channels of the Yangtze Estuary is presented in Figure 2. Colored boxes in each bar represent the subtidal transport components in one channel. The colors indicate the contributions of the individual processes and the black line shows the sum of all contributions. Positive numbers indicate net downstream transport. The leading order river flow contributes the most to the NWT in each branch, except for the North Branch (NB), which is the shallowest and the narrowest channel.

The directions of each component of the NWT in all channels are identical to those found by Alebregtse and de Swart (2016), except for the transport due to baroclinic forcing (baroc) and the first order correction to river flow (rivc), which are not considered in their model. However, the magnitude of each transport component is different. The NWT due to velocity-depth asymmetry (vda) and Stokes and its associated return flow (Stokes) are larger compared to Alebregtse and de Swart (2016), which implies that a 1D model may underestimate the transport related to flow vertical structure.

The superposition of the various contributions leads to the negative NWT in the NB. This has also been observed (Wu et al., 2006; Li et al., 2010; W. Zhang et al., 2017). Wu et al. (2006) concluded that the negative transport is the consequence of the funnel-shaped bottom of the NB and the river-tide interaction locally near the junction. However, in our model, the geometric characteristics are extremely simplified and small-scale dynamics near the junctions is not resolved. The recreation of landward NWT in the NB with this model therefore suggests that it is the consequence of hydrodynamical processes over a much larger spatial scale and hence a robust feature. We further add that this is mainly due to two kinds of tidal rectification processes: Stokes and its return flow and velocity-depth asymmetry. This is because the NB is the shallowest channel with the largest tidal range, causing both the total depth ($H + \eta$) and velocity highly asymmetric between high water and low water. The numerical results of W. Zhang et al. (2017) showed that, during the dry season, the averaged NWT in the NB excluding the river water transport is about $-1{,}500$ m^3/s, which is comparable to our model results, about $-1{,}200$ m^3/s. Using the factor separation method (Stein & Alpert, 1993), they decomposed the flow discharge into three components: river, tide, and river-tide interaction. The transport due to the tide was subsequently decomposed into Stokes transport, return flow transport, and a residual term. They showed that the Stokes transport and the return flow transport should be the processes that are most responsible for the negative NWT in the NB. It is important to realize that the factor separation method is intrinsically different from the decomposition presented in this study. The transport by Stokes return flow in W. Zhang et al. (2017) contains all the transport components due to tidal rectification in this study. Hence, their findings also support the results of the present study.

3.2. Wet Season

River water transport in each channel increases linearly with the river discharge from the Yangtze River (YR) and therefore the river water diversion ratio, the diversion ratio when river water transport is the only contribution to NWT, is unaffected by the prescribed discharge (J. Wang et al., 2021). All other contributions to the NWT are not sensitive to the river discharge (not shown). First, this is because the tidal rectification terms are mostly driven by the leading order tide, and the tide-river interaction is minor in the downstream part of the estuary (J. Wang et al., 2021). Second, even though the salt intrusion limits move seaward for increasing river discharge, the net transport due to baroclinic pressure is insensitive to river discharge because the salt intrusion limits do not move across the junctions. This is explained in Appendix A. Third, the correction to river flow is forced by river discharge. This contribution is therefore most sensitive to river discharge among insensitive first order contributions.

The sensitivity of the net water diversion ratio (nWDR) to the discharge from the YR at three junctions is contained in Figure 3a. At every junction, results are shown for one of the two downstream channels, as the value of nWDR for the other channel can be obtained by subtracting the value in this figure from unity. The nWDR for the North Branch (NB) changes sign from negative to positive when the prescribed discharge is about 1.7×10^4 m^3/s, meaning that the NWT in the NB changes direction from landward to seaward. This is because, for increasing river discharge, all subtidal transport components change very little, except the river discharge itself, which is directed seaward. It can also be seen that a larger river discharge leads to a more even distribution of the nWDR, which confirms the finding of Li et al. (2010). Specifically, for increasing river discharge, the nWDR converges to the diversion ratio of river discharge. The reason for this is, again, other transport components are not sensitive to increasing river discharge. This is further illustrated in panels (b), (c), and (d), which show the components of nWDR at the NB, the NC, and the NP, respectively. Black curves are the nWDR as in panel (a). Other curves represent the fractions of the associated NWT component, and they add up to the black curve in each panel. Increasing discharge, the relative contributions of the first order components decrease, and the nWDR (black line) converges to the river contribution (beige line).

3.3. Spring-Neap Tide

The river water transport is not sensitive to the prescribed tidal amplitude (J. Wang et al., 2021). For the baroclinic contribution to the net transport, it will be argued in Appendix A that the NWT is insensitive to changes in our model configuration of the Yangtze Estuary, so K_h is kept constant. Still, the baroclinic contribution to the NWT decreases under larger tidal forcing amplitudes, because larger tidal amplitudes cause larger vertical eddy viscosity, which reduces the gravitational circulation induced by the horizontal density gradient. Naturally, the components that are forced by the tides (advection, Stokes, velocity-depth asymmetry, and dynamic pressure) are sensitive to the tidal amplitude and their magnitudes increase almost linearly for larger tidal amplitudes. The

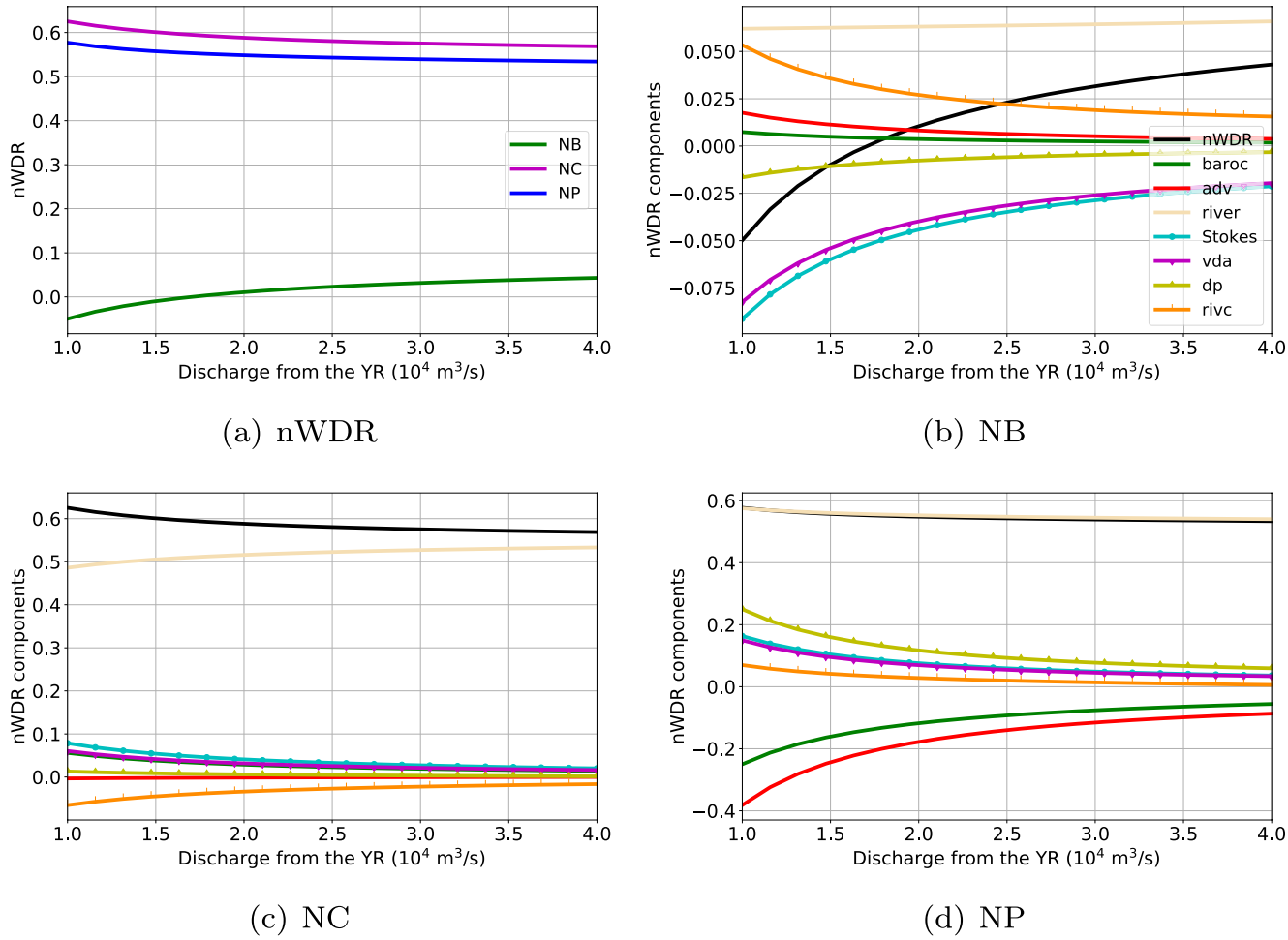

Figure 3. Sensitivity of net water diversion ratio (nWDR) and its component to river discharge from the Yangtze River (YR). (a) nWDR in the NB, the NC, and the NP versus discharge from the Yangtze River. (b) Contribution of each subtidal flow to the nWDR of the NB (branching point i_1). Black curve is the nWDR of the NB as in (a). (c) As (b), but for the NC (branching point i_2). (d) As (b), but for the NP (branching point i_3).

first order correction to river water transport is also sensitive to the tidal amplitude as tides affect the generation of turbulence. Its magnitude decreases in the North Passage, the South Passage, and the South Channel, while transport increases in the other channels.

From neap to spring tide, the net water diversion ratio (nWDR) for the North Passage (NP) is almost doubled (Figure 4a). This is the result of the cumulative change in all first order contributions to the subtidal transport (panel d). For increasing tidal amplitudes, the decrease in Q_{rivc} in the NP is similar to that in the South Branch (SB, not shown). This suggests that the changes in Q_{rivc} in the South Passage (SP) and the North Channel (NC) compensate each other, that is, a redistribution of river water. Therefore, for larger tidal forcing at subtidal timescale, less river water is exported from the NP and this amount of water is exported through the North Branch (NB). The net transport direction in the NB changes sign from neap to spring tide, which again confirms that the landward transport in the NB during dry season is mostly due to tidal rectification processes and hence is weak or absent during neap. The nWDR of the NC is less sensitive (panel c).

3.4. Deep Waterway Project

The combined effects of deepening and narrowing on NWT are shown in Figure 5. This figure is similar to Figure 2 but shows the difference in NWT compared to the case before the DWP. The total difference in the NWT is attached to the left of each bar and indicated by a black vertical line.

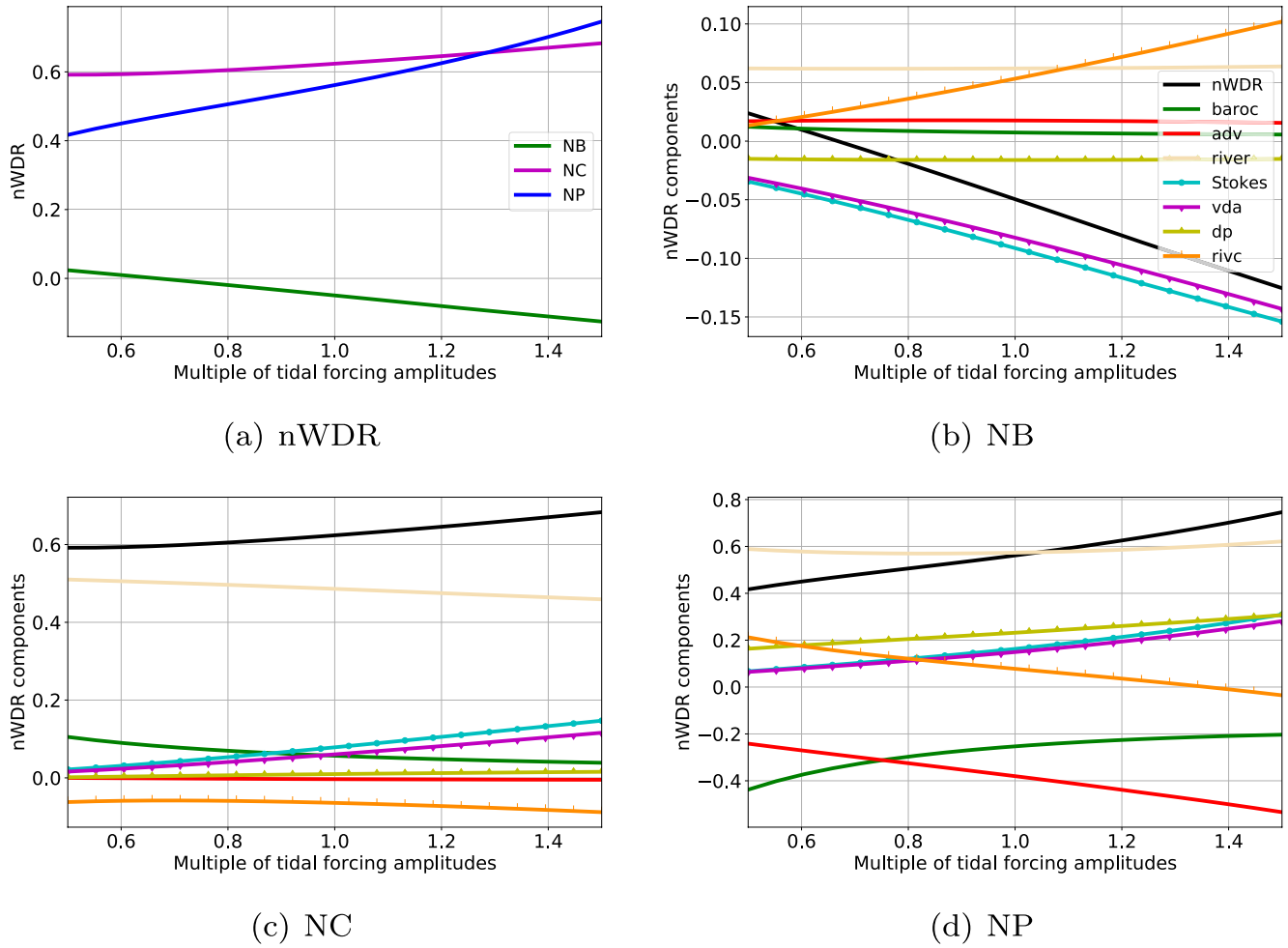

Figure 4. As Figure 3, but for sensitivity of net water diversion ratio (nWDR) to multiple of tidal forcing amplitudes at the sea.

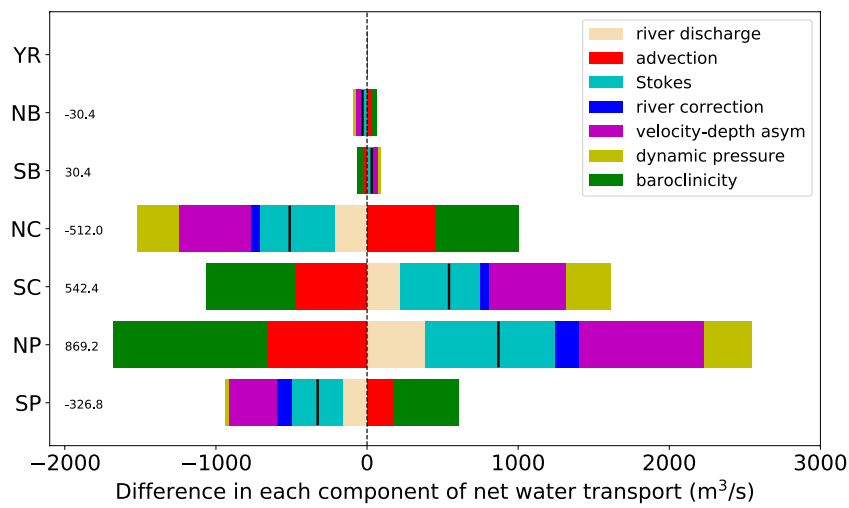

Figure 5. Effect of the DWP on each component of the NWT. Each box represents the difference in the corresponding subtidal transport component between after and before the construction of the DWP. The value on the left of each bar is the sum of all boxes in the bar, that is, the difference in the NWT (m^3/s). In each channel, the change in the NWT is also indicated by a black vertical line.

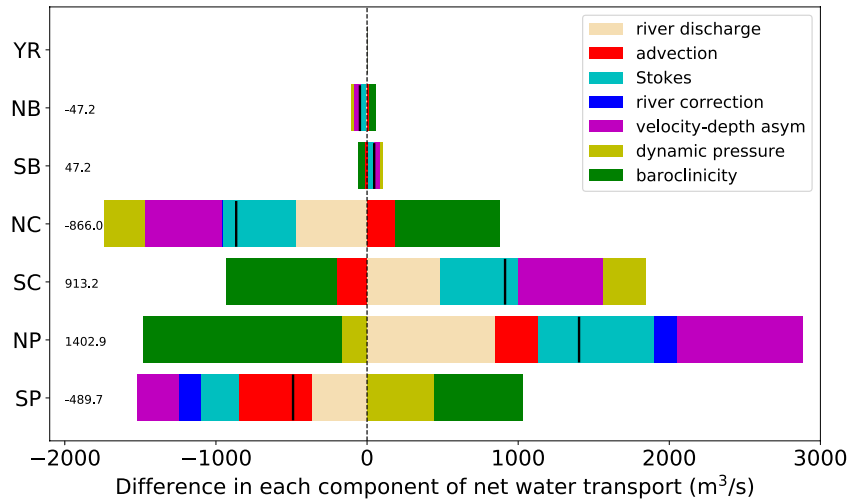

(a) Deepening

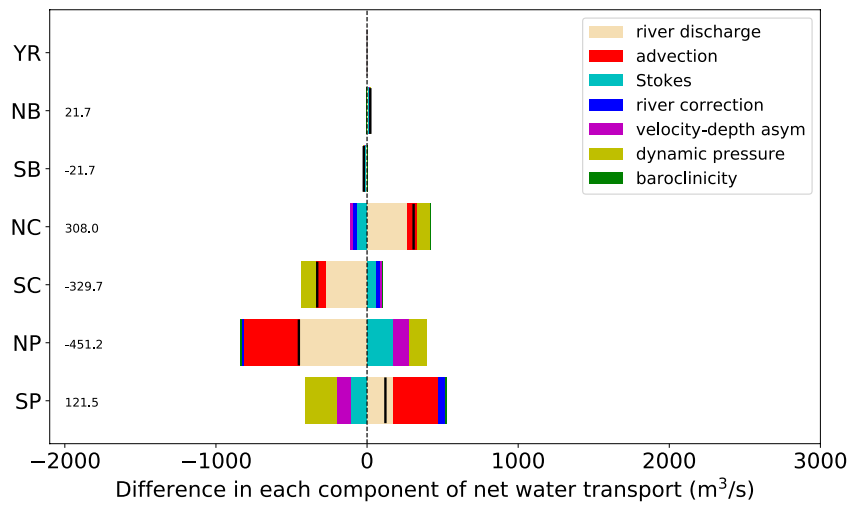

(b) Narrowing

Figure 6. As Figure 5, but for difference in subtidal transport components between after and before only dredging (a) and only narrowing (b) in the NP.

The effect of the construction of the DWP was local, as the NWTs in the North Branch and the South Branch were hardly affected. The DWP increased the NWT in the North Passage (NP). This was caused by several different mechanisms. First, river water transport was redistributed over channels due to the geometric changes caused by the DWP. After the DWP, less river water was transported into the North Channel (NC) and the South Passage (SP). They were discharged into the sea through the NP. Second, the subtidal transport due to continuous dynamic pressure changed in the same way as the river discharge and the magnitude was also comparable. However, the contribution of the redistribution by river discharge and dynamic pressure was small compared to those arising from two tidal rectification processes, Stokes and velocity-depth asymmetry. Both of the two tidal rectification processes contributed to the change in the subtidal transport in the same way as the river discharge, while the magnitude of each of them was more than twice as large as that of the river flow. This pattern was largely compensated by the transport due to momentum advection and density-driven flow.

The effects of only deepening and only narrowing of the NP on NWT are contained in Figure 6a and 6b, respectively. Overall, the effect of narrowing on NWT was much less strong but opposite to the effect of dredging. This is because deepening and narrowing had opposite effects on the channel cross-section area. For larger water depth in the NP (panel a), density-driven flow was stronger in the NP and thereby induced more landward transport. It

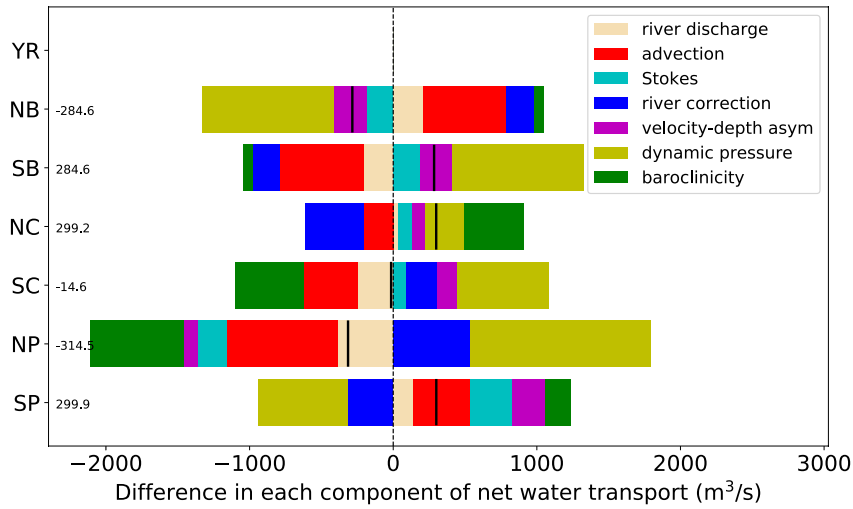

Figure 7. As Figure 5, but for the difference of subtidal transport components between after and before 2 m sea level rise.

can be seen that the changes in the transport due to Stokes and velocity-depth asymmetry, the two most significant tidal rectification processes that both increased the transport in the NP, were due to the deepening. The reason for the same response of the transport due to Stokes and velocity-depth asymmetry to deepening and narrowing can be understood with the transport mechanism provided in Section 4.1. On the other hand, the effect of narrowing in the NP (panel b) was less significant. The effect of narrowing was the same as described by (Y. Wang et al., 2010): the NWT in the NP was decreased and redirected to the South Passage (SP) and the North Channel through the South Channel, because the amount of NWT reduced in the NP (with respect to before the narrowing) has to be discharged into the sea to fulfill mass conservation. This is due to the change in river discharge, as other transport contributions almost cancel with each other. It should be noted that the sum of Figures 6a and 6b is qualitatively but not quantitatively the same as Figure 5. This is because narrowing has a different quantitative effect on a channel of 7 m depth, which is shown here, and 11 m depth. For this reason, the magnitude reduction in the transport due to advection in Figure 6b is smaller than that in Figure 5. This implies that the effect of narrowing on subtidal transport is larger for a deeper channel.

3.5. Sea Level Rise

Each subtidal transport component is sensitive to SLR (Figure 7). For each channel, subtidal transport induced by the density-driven flow is larger in magnitude after sea level rise, because the density-driven flow scales with depth. SLR enhances the transport due to advection in the North Passage, the South Passage, and the North Branch, while greatly canceled by the transport induced by the dynamic pressure. Qualitatively, the effect of SLR on the subtidal transport due to Stokes and velocity-depth asymmetry is the same for all channels.

The net effect of sea level rise (SLR) on net water diversion ratio (nWDR) is, however, not too sensitive (Figure 8a). This is mainly due to the effect of SLR on different transport components canceling each other, such as the cancellation between advection and dynamic pressure in the North Branch (panel b). In the North Passage (NP, panel d), the sum of density-driven flow and advection together canceled by the sum of dynamic pressure and first order river flow, resulting in the curve for nWDR is almost parallel to the curve for Stokes and velocity-depth asymmetry. Although each transport component in the North Channel (NC) is sensitive to SLR, their contributions to the nWDR are not sensitive (panel c) because their magnitudes are not comparable to the NWT in the NC. This conclusion is specific for the Yangtze and the effect of SLR on nWDR in other networks could be different, depending on the relative importance of the various mechanisms.

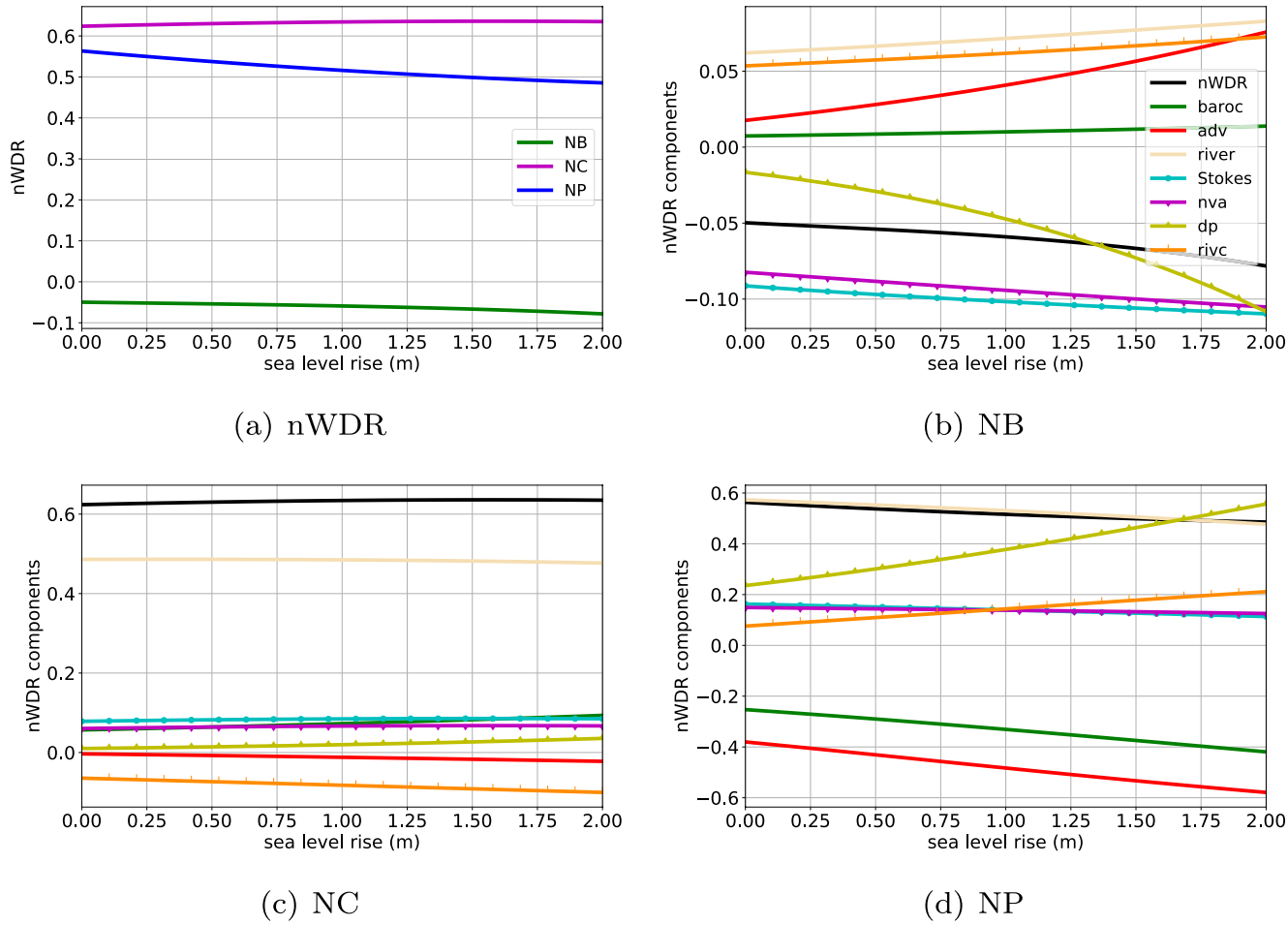

Figure 8. As Figure 3, but for sensitivity of net water diversion ratio (nWDR) to sea level rise.

4. Discussion

4.1. Net Water Transport Mechanism in Networks

The decomposition of net water transport (NWT) discussed in this study yields a natural extension of the theory of differential water level setup of Sassi et al. (2011) that explains the effect of tides on NWT. They found that tides affect the subtidal water level in channels and thereby modifies the subtidal pressure gradient at junctions. This reallocates the river discharge at junctions from channels with a relatively high setup to channels with a lower setup until the setup is equal. This conclusion was drawn from considering the difference between the subtidal water level with and without tides. It therefore describes the net effect of tides, which contains all the forcing mechanisms that are related to tides in this study. Here, it will be shown that this theory can be generalized to explain the creation of NWT by arbitrary subtidal forcing, which also contain the net effect of tides, in estuarine networks.

Any type of subtidal forcing within a channel will be reflected in the subtidal momentum balance through two terms: the barotropic pressure gradient due to surface elevation and the internal friction (Equation 12a). Here, we focus on the first: the pressure gradient. Now consider a three-channel system with one river channel and two sea channels, as depicted in Figure 9. As a consequence of mass conservation, the net transport in the river channel is always the same as the imposed river discharge. This means that for any subtidal forcing, net transport can only be generated in the two sea channels. The subtidal forcing in each channel directly leads to a barotropic pressure gradient and thereby subtidal water level setup (or set down), as illustrated by the black curves in Figure 9. At the junction, this setup/set down from both channels is, in general, discontinuous. To compensate this discontinuity in pressure gradient at the junction, there must exist additional subtidal transport. This causes a setup in the

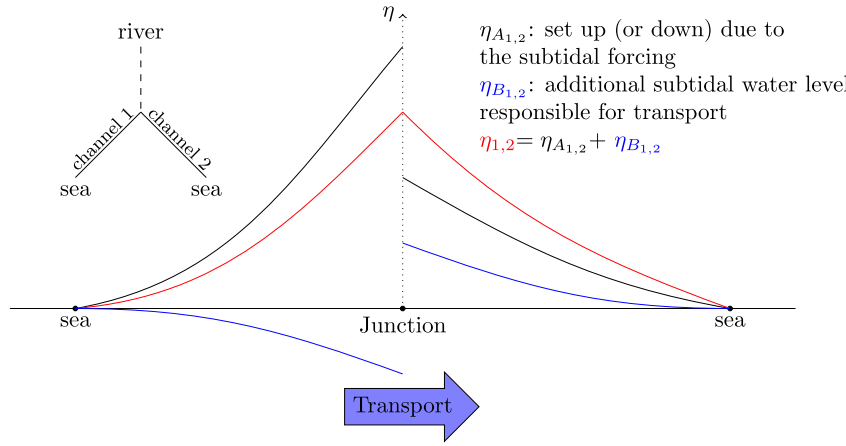

Figure 9. A conceptual figure shows the subtidal transport mechanism in a network of three channels. The two sea channels are labeled by 1 and 2. Black curves are the subtidal water level (subscript *A*) as the response to the subtidal forcing. Blue curves are the subtidal water level (subscript *B*) due to the subtidal transport, forced by the pressure difference at the junction created by the black curves. The total subtidal water level (red) is continuous. Note that the subtidal water level is the same as the mean sea level at the sea.

receiving channel and a set down in the other channel (blue curves) such that the total subtidal water level (red curves) is continuous at the junction. Hence, the theory of differential water level setup can actually be applied to each of the contributions identified in this study.

This mechanism can also be seen from the analytical solutions to all subtidal flows (see Section S4 in the Supporting Information S1). For example, taking the limit of no-slip condition, the barotropic pressure gradient in the solution to the density-driven flow depends on the unknown water transport Q_{baroc}:

$$\frac{\mathrm{d}}{\mathrm{d}x}\eta_{\text{baroc}} = -\frac{3\check{A}_{v0}^{\,0}}{gH^2}\left(\frac{2gH^3\beta_s}{\check{A}_{v0}^{\,0}}\frac{\mathrm{d}s}{\mathrm{d}x} + \frac{Q_{\text{baroc}}}{b(x)H}\right). \tag{18}$$

By integrating along the channel, on the right-hand side, the first term yields the subtidal water level of density-driven flow (black curves in Figure 9) induced by the subtidal forcing (salinity gradient induced baroclinic pressure gradient force), the second term gives the subtidal water level responsible for the transport (blue curves in Figure 9), and there is an unknown integration constant that needs to be determined together with the unknown transport Q_{baroc} using the channel matching and boundary conditions (Equation 14) such that mass is conserved and subtidal water level is continuous at junctions. The solution to the density-driven flow in channels of a network is

$$u_{\text{baroc}} = \frac{gH^3\beta_s}{48\check{A}_{v0}^{\,0}}\left(1 - 9\left(\frac{z}{H}\right)^2 - 8\left(\frac{z}{H}\right)^3\right)\frac{\mathrm{d}s}{\mathrm{d}x} + \frac{Q_{\text{baroc}}}{b(x)H}\left(\frac{3}{2} - \frac{3}{2}\left(\frac{z}{H}\right)^2\right), \tag{19}$$

which contains two parts. The first term is the classical solution to the density-driven flow in a single channel (Hansen & Rattray, 1965). It is zero after averaging over depth and hence does not contribute to transport. The second term, which shares the same structure as the river flow (Ianniello, 1977), has the depth-averaged value of transport per unit cross sectional area and therefore is responsible for the transport. The special case is the subtidal contribution by continuous dynamic pressure at junctions: it is essentially forced by the difference in the momentum advection at junctions (see Section S5 in the Supporting Information S1 for details) and hence not an internal forcing spread over an entire channel. Similar to the river discharge, it is an external forcing for every channel (black curve is null), but the transport is distributed such that the leading order momentum is conserved at junctions.

Note that every contribution to the NWT is created at the global scale: the transport created by each driver is determined by the associated setup (or set down) over all channels. Therefore, it is not the local properties at junctions that are important, but the flow in all of the channels throughout the estuarine network.

4.2. Generalization and Limitations

The method used in this study is generic and therefore some results can be generalized. First, in any estuarine network where the river-tide interaction is relatively weak, the sensitivity of NWT to river discharge reflects that of the river discharge contribution only, as other contributions to the net transport are mostly generated by tides. Second, in such estuaries larger tidal amplitudes will typically reduce the transport created by the gravitational circulation. Moreover, the magnitude of each contribution to NWT due to tides is expected to be positively correlated to the tidal amplitudes. Their net effect is hence the consequence of the balance of all these contributions in different channels. Hence, this is strongly dependent on the estuary under consideration. In general, such a network needs to be analyzed globally rather than focusing on one or some of the channels, or on local dynamics near a junction.

The idealized nature of the model imposes some limitations, some of which are discussed in J. Wang et al. (2021). These include for example, instantaneous adjustment of the system to time-varying forcing (Geyer & MacCready, 2014) and the simplified geometry that does not explicitly resolve lateral process (Scully et al., 2009) and tidal flats (Hepkema et al., 2018). Also the effect of changing vertical density stratification is not dynamically resolved. The baroclinic pressure assumes negligible vertical stratification and the eddy viscosity assumes a small prescribed vertical tidal density gradient that may no longer be representative if the estuary becomes more strongly stratified. This may for example, occur around neap tide, under large channel deepening, or sea level rise. Nonetheless, the model result is not sensitive to the vertical density difference (see Section S3.1 and Figure S1 in the Supporting Information S1). A more complex description of density-dependent and time-dependent eddy viscosity, as well as internally generated overtides, may be added to this framework to enhance complexity and realism, which is beyond the scope of this study.

5. Conclusions

Using a process-based model, the net water transport (NWT) in channels of estuarine networks is disentangled and attributed to various physical processes and drivers: the river discharge, vertically well-mixed salinity induced along-channel density gradient, Stokes transport and its return flow, advection of horizontal momentum, velocity-depth asymmetry, and continuous dynamic pressure at junctions. The mechanism for the distribution of NWT of each physical driver is explained by generalizing the conceptual framework of differential water level setup.

The model is subsequently applied to the Yangtze Estuary, a typical estuarine network, to investigate the sensitivity of the distribution of NWT over its channels to river discharge, spring-neap modulation, local deepening and narrowing, and sea level rise. Besides the river water transport itself, NWT due to other physical drivers are quantitatively insensitive to prescribed river discharge; drivers related to tide only change slightly due to weak tide-river interaction and the baroclinic transport is weakly dependent on salt intrusion. Hence, for increasing river discharge, the distribution of NWT converges to the river water distribution. Conversely, the river discharge distribution is less sensitive to the transport driven by tide and density gradients. Notably, assuming a stationary spring/neap state (instantaneous hydrodynamic adjustment), by varying the tidal forcing from neap to spring tide, the direction of NWT in the North Branch changes from seaward to landward because of tidal rectification processes. It was found that deepening and narrowing of a channel have opposite effects on NWT. The effect of the Deep Waterway Project in the Yangtze Estuary was dominated by the deepening, leading to increased NWT in the North Passage. Each identified driver is sensitive to sea level rise. However, in the model configuration of the Yangtze Estuary, the canceling of components against each other causes the NWT in each channel of the Yangtze to be not so sensitive to sea level rise up to 2 m, with a maximum decrease in the North Passage of about 20%.

Appendix A: Sensitivity of Baroclinicity Transport to Horizontal Diffusivity

In contrast to a single channel, in which the transport is independent of the salinity (Cheng et al., 2010; Dijkstra et al., 2017), in channels of a network, however, the transport due to density-driven flow depends on the salinity, for which salinity equation (Equation 4) is employed. To test the sensitivity of the baroclinic transport to salinity, horizontal diffusivity K_h varied between 50 and 1,200 m^2/s. The resulting salinity is compared to the observation made by E. Zhang et al. (2011) [Figure A1(a)]. This shows that the bounds on K_h envelope the observations and

thus capture the uncertainty. However, in all channels of the network, the net water transport induced by the baroclinic forcing is not sensitive to the value of K_h [Figure A1(b)]. This lack of sensitivity can be easily explained with the subtidal transport mechanism for networks. The subtidal water level created by the baroclinic forcing in each channel [Figure A1(c)] is not continuous at branching points and therefore results in pressure difference at vertex points. A barotropic pressure needs to compensate this and creates additional return flow that generates the subtidal transport. Although larger value of K_h leads to longer salt intrusion length, the salt intrusion limit (e.g., 1 psu) in most channels is still bounded within each channel. The baroclinic pressure built up in one channel depends on the salinity difference at the ends of the channel and hence hardly changes with K_h [Figure A1(c)]. This in turn leads to net water transport because baroclinic forcing remains the same for different K_h. In other words, for a well-mixed estuary, as long as the salt intrusion limit does not move significantly from one channel to another, the influence of K_h on the net water transport is negligible. In the North Passage (NP), for K_h larger than 500 m^2/s, the salt intrusion limit moves to the South Branch and thereby causes the transport in the NP to slightly increase. Following the same reason, increasing river discharge causes the salt intrusion limits to move further seaward such that these limits remain in the sea channels and hence, the transport due to density-driven flow is unaffected.

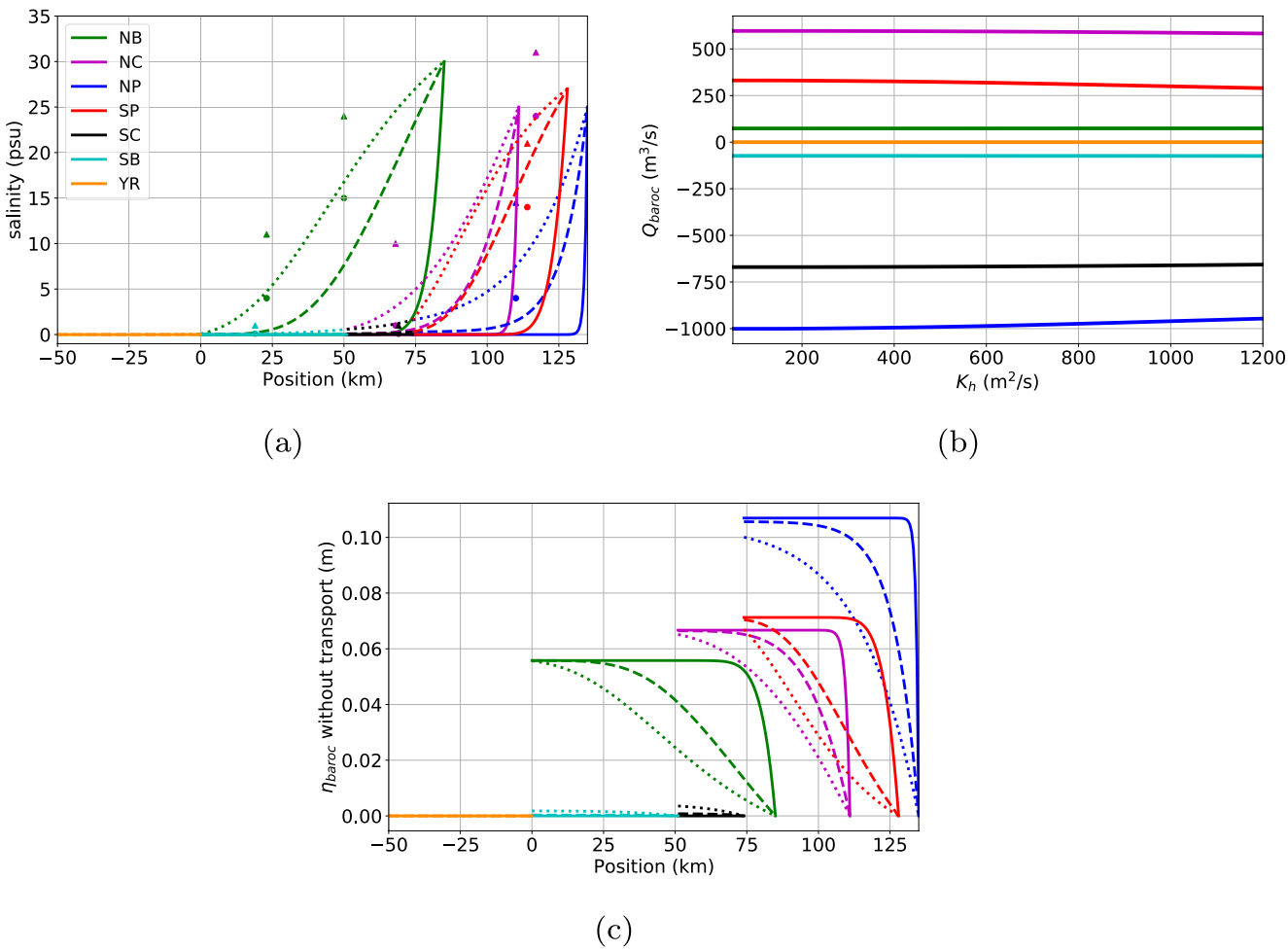

Figure A1. (a) Tidally averaged salinity profile for the reference case computed with K_h = 50 m^2/s (dotted), K_h = 500 m^2/s (solid), and K_h = 1,200 m^2/s (dashed). Dots (triangles) are measurements made at low (high) water slack (E. Zhang et al., 2011). (b) Sensitivity of the net water transport induced by baroclinic forcing to K_h. (c) Subtidal water level directly created the baroclinic forcing in each channel for different K_h. Water levels at the seaward side of each channel are set to 0.

Data Availability Statement

The model is described in Section 2 and in Supporting Information S1. The model parameters for the Yangtze Estuary are provided in Table 1. The model used for this study is made available in a public repository at https://doi.org/10.5281/zenodo.5752484.

Acknowledgments
This research was funded by the Dutch Research Council (NWO) (Grant ALWSW.2016.012). The authors thank Prof. Heqin Cheng of East China Normal University and Dr. Chenjuan Jiang of Yangzhou University, who provided important input and suggestions for this study. We also thank two anonymous reviewers for the comments that improved this manuscript.

References

Alebregtse, N. C., & de Swart, H. E. (2016). Effect of river discharge and geometry on tides and net water transport in an estuarine network, an idealized model applied to the Yangtze Estuary. *Continental Shelf Research*, *123*, 29–49. https://doi.org/10.1016/j.csr.2016.03.028

Buschman, F. A., Hoitink, A. J. F., van der Vegt, M., & Hoekstra, P. (2010). Subtidal flow division at a shallow tidal junction. *Water Resources Research*, *46*(12). https://doi.org/10.1029/2010WR009266

Chen, W., & de Swart, H. E. (2016). Dynamic links between shape of the eddy viscosity profile and the vertical structure of tidal current amplitude in bays and estuaries. *Ocean Dynamics*, *66*(3), 299–312. https://doi.org/10.1007/s10236-015-0919-6

Cheng, P., Valle-Levinson, A., & de Swart, H. E. (2010). Residual currents induced by asymmetric tidal mixing in weakly stratified narrow estuaries. *Journal of Physical Oceanography*, *40*(9), 2135–2147. https://doi.org/10.1175/2010JPO4314.1

Cloern, J. E., Abreu, P. C., Carstensen, J., Chauvaud, L., Elmgren, R., Grall, J., et al. (2016). Human activities and climate variability drive fast-paced change across the world's estuarine–coastal ecosystems. *Global Change Biology*, *22*(2), 513–529. https://doi.org/10.1111/gcb.13059

Dijkstra, Y. M., Brouwer, R. L., Schuttelaars, H. M., & Schramkowski, G. P. (2017). The iFlow modelling framework v2.4: A modular idealized process-based model for flow and transport in estuaries. *Geoscientific Model Development*, *10*(7), 2691–2713. https://doi.org/10.5194/gmd-10-2691-2017

Engelund, F. (1970). Instability of erodible beds. *Journal of Fluid Mechanics*, *42*(2), 225–244. https://doi.org/10.1017/S0022112070001210

Geyer, W. R., & MacCready, P. (2014). The estuarine circulation. *Annual Review of Fluid Mechanics*, *46*(1), 175–197. https://doi.org/10.1146/annurev-fluid-010313-141302

Godin, G. (1999). The propagation of tides up rivers with special considerations on the upper Saint Lawrence River. Estuarine. *Coastal and Shelf Science*, *48*(3), 307–324. https://doi.org/10.1006/ecss.1998.0422

Hansen, D. V., & Rattray, M., Jr. (1965). Gravitational circulation in straits and estuaries. *Journal of Marine Research*, *23*(104–122).

Hepkema, T. M., de Swart, H. E., Zagaris, A., & Duran-Matute, M. (2018). Sensitivity of tidal characteristics in double inlet systems to momentum dissipation on tidal flats: A perturbation analysis. *Ocean Dynamics*, *68*(4), 439–455. https://doi.org/10.1007/s10236-018-1142-z

Hill, A. E., & Souza, A. J. (2006). Tidal dynamics in channels: 2. Complex channel networks. *Journal of Geophysical Research: Oceans*, *111*(C11). https://doi.org/10.1029/2006JC003670

Hoitink, A., & Jay, D. (2016). Tidal river dynamics: Implications for deltas. *Reviews of Geophysics*, *54*, 240–272. https://doi.org/10.1002/2015RG000507

Ianniello, J. P. (1977). Tidally induced residual currents in estuaries of constant breadth and depth. *Journal of Marine Research*, *35*, 755–786.

Ianniello, J. P. (1979). Tidally induced residual currents in estuaries of variable breadth and depth. *Journal of Physical Oceanography*, *9*(5), 9622–9974. https://doi.org/10.1175/1520-0485(1979)009<0962:TIRCIE>2.0.CO;2

Jiang, C., de Swart, H., Li, J., & Liu, G. (2013). Mechanisms of along-channel sediment transport in the North Passage of the Yangtze Estuary and their response to large-scale interventions. *Ocean Dynamics*, *63*, 283–305. https://doi.org/10.1007/s10236-013-0594-4

Jiang, C., Li, J., & de Swart, H. E. (2012). Effects of navigational works on morphological changes in the bar area of the Yangtze Estuary. *Geomorphology*, *139–140*, 205–219. https://doi.org/10.1016/j.geomorph.2011.10.020

Kuang, C., Liang, H., Mao, X., Karney, B., Gu, J., Huang, H., et al. (2017). Influence of potential future sea-level rise on tides in the China Sea. *Journal of Coastal Research*, *33*(1), 105–117. https://doi.org/10.2112/JCOASTRES-D-16-00057.1

Kundu, P. K., Cohen, I. M., & Dowling, D. R. (2016). In P. K. Kundu, I. M. Cohen, & D. R. Dowling (Eds.), *Fluid mechanics* (6th ed.). Academic Press.

Li, L., Zhu, J., Wu, H., & Wang, B. (2010). A numerical study on water diversion ratio of the Changjiang (Yangtze) estuary in dry season. *Chinese Journal of Oceanology and Limnology*, *28*(3), 700–712. https://doi.org/10.1007/s00343-010-9114-2

Lu, S., Tong, C., Lee, D.-Y., Zheng, J., Shen, J., Zhang, W., & Yan, Y. (2015). Propagation of tidal waves up in Yangtze Estuary during the dry season. *Journal of Geophysical Research: Oceans*, *120*(9), 6445–6473. https://doi.org/10.1002/2014JC010414

Nicholls, R. J., Marinova, N., Lowe, J. A., Brown, S., Vellinga, P., de Gusmão, D., et al. (2011). Sea-level rise and its possible impacts given a "beyond 4°C world" in the twenty-first century. *Philosophical Transactions of the Royal Society A: Mathematical, Physical & Engineering Sciences*, *369*, 161–181. https://doi.org/10.1098/rsta.2010.0291

Pritchard, D. W. (1954). A study of the salt balance in a coastal plain estuary. *Journal of Marine Research*.

Ridderinkhof, H. (1988). Tidal and residual flows in the western Dutch Wadden Sea II: An analytical model to study the constant flow between connected tidal basins. *Netherlands Journal of Sea Research*, *22*(3), 185–198. https://doi.org/10.1016/0077-7579(88)90022-1

Sassi, M. G., Hoitink, A. J. F., de Brye, B., Vermeulen, B., & Deleersnijder, E. (2011). Tidal impact on the division of river discharge over distributary channels in the Mahakam Delta. *Ocean Dynamics*, *61*(12), 2211–2228. https://doi.org/10.1007/s10236-011-0473-9

Scully, M. E., Geyer, W. R., & Lerczak, J. A. (2009). The influence of lateral advection on the residual estuarine circulation: A numerical modeling study of the Hudson river estuary. *Journal of Physical Oceanography*, *39*(1), 107–124. https://doi.org/10.1175/2008JPO3952.1

Soulsby, R. (1997). *Dynamics of marine sands. a manual for practical applications*. Thomas Telford.London.

Stein, U., & Alpert, P. (1993). Factor separation in numerical simulations. *Journal of the Atmospheric Sciences*, *50*(14), 21072–22115. https://doi.org/10.1175/1520-0469(1993)050<2107:FSINS>2.0.CO;2

van de Kreeke, J. (1988). Hydrodynamics of tidal inlets. In D. G. Aubrey, & L. Weishar (Eds.), *Hydrodynamics and sediment dynamics of tidal inlets hydrodynamics and sediment dynamics of tidal inlets* (Vol. 29, pp. 1–23). Springer-Verlag. https://doi.org/10.1029/ln029p0001

Wang, J., de Swart, H. E., & Dijkstra, Y. M. (2021). Dependence of tides and river water transport in an estuarine network on river discharge, tidal forcing, geometry and sea level rise. *Continental Shelf Research*, *225*, 104476. https://doi.org/10.1016/j.csr.2021.104476

Wang, Y., Shen, J., & He, Q. (2010). A numerical model study of the transport timescale and change of estuarine circulation due to waterway constructions in the Changjiang Estuary, China. *Journal of Marine Systems*, *82*(3), 154–170. https://doi.org/10.1016/j.jmarsys.2010.04.012

Wu, H., Zhu, J., Chen, B., & Chen, Y. (2006). Quantitative relationship of runoff and tide to saltwater spilling over from the North branch in the Changjiang estuary: A numerical study. *Estuarine, Coastal and Shelf Science*, *69*(1), 125–132. https://doi.org/10.1016/j.ecss.2006.04.009

Yang, Z., Cheng, H., & Li, J. (2015). Nonlinear advection, Coriolis force, and frictional influence in the South channel of the Yangtze estuary, China. *Science China Earth Sciences*, *58*(3), 429–435. https://doi.org/10.1007/s11430-014-4946-9

Zhang, E., Savenije, H. H., Wu, H., Kong, Y., & Zhu, J. (2011). Analytical solution for salt intrusion in the Yangtze Estuary, China. *Estuarine, Coastal and Shelf Science*, *91*(4), 492–501. https://doi.org/10.1016/j.ecss.2010.11.008

Zhang, W., Feng, H., Hoitink, A., Zhu, Y., Gong, F., & Zheng, J. (2017). Tidal impacts on the subtidal flow division at the main bifurcation in the Yangtze River Delta. Estuarine. *Coastal and Shelf Science*, *196*, 301–314. https://doi.org/10.1016/j.ecss.2017.07.008